Dalton Transactions

PAPER

View Article Online
View Journal | View Issue

Cite this: *Dalton Trans.*, 2025, **54**, 12806

DFT insights into the bifunctional nature of a bioinspired tungsten complex

Miljan Z. Ćorović,[a] Maria José Calhorda,[b] Nuno A. G. Bandeira *[b] and Nadia C. Mösch-Zanetti *[a]

Received 1st July 2025,
Accepted 4th August 2025

DOI: 10.1039/d5dt01544h

rsc.li/dalton

Tungsten model complexes that replicate aspects of enzymatic activity are scarce due to challenges in reducing the readily prepared WO_2^{2+} moiety. As a result, studies of bioinspired catalytic cycles remain limited, since tungsten in nature primarily facilitates redox processes such as Oxygen Atom Transfer (OAT). In our group, we recently observed that pyridine-2-thiolate (PyS)-supported tungsten dioxido complexes can be reduced to phosphine-stabilized W(IV) compounds, opening up opportunities for investigating rarely observed reduced participants in the OAT catalytic cycles. Reactivity studies revealed the activation of DMSO – an expected oxotransferase substrate, and O_2 – a substrate typically associated with oxygenase enzymes. The activation of the latter encouraged a detailed computational DFT study (ORCA/PBE0-D4). Although heavy elements like tungsten usually remain in diamagnetic spin states, our findings indicate that O_2 is activated by $[WO(PyS)_2(PMe_3)]$ in two successive steps, binding as η^1-$(O_2)^-$ in a paramagnetic W(V) intermediate, which converts to a much more stable diamagnetic W(V) species after spin crossover. The oxidation to W(VI) is triggered by the η^1- to η^2-haptotropic shift of O_2. This complex converts to the W(VI) dioxide with the highest energy barrier of the O_2 activation reaction ($\Delta G^\ddagger$ 93 kJ mol^{-1}), but the regeneration of the catalytic W(IV) species is even more difficult ($\Delta G^\ddagger$ 118 kJ mol^{-1}). The high coordination flexibility of the ancillary PyS ligands is key to reaching different spin states, which are essential for dioxygen activation. Interestingly, the observed reactivity may resemble the inactivation pathway of tungsten enzymes under aerobic conditions.

Introduction

A single transition metal center can support a variety of catalytic transformations. Given the constant climatic and environmental changes, nature has taken advantage of this adaptability throughout evolution.[1,2] The most abundant transition metals in biological systems are primarily found in the first row.[3] However, nature sometimes selects heavier elements such as Mo or W, due to their ability to support two-electron transfer reactions.[4–6] These metals predominantly catalyze Oxygen Atom Transfer (OAT) reactions. The incorporation of an oxygen atom into a biological substrate can be facilitated by oxygenases, which activate molecular oxygen (O_2) to insert one or both of its atoms into the substrate—commonly yielding hydroxylated products,[7] or by oxotransferases, which mediate the transfer of an oxygen atom from alternative O-donors such as water, nitrate, or sulfoxides, to the substrate.[8]

A deeper understanding of the natural selection of transition metals and the enzymatic mechanisms of metalloenzymes is often achieved by the study of bioinspired model systems.[9] Those for oxygenases are of general interest in catalysis due to their ability to utilize O_2, the ultimate green oxidant, which inspired many research groups to investigate systems mainly based on iron[7,10–15] and copper.[16,17] In addition to experimental approaches, theoretical investigations play a crucial role in elucidating the chemistry of these models, particularly in characterizing transient intermediates that remain inaccessible to conventional experimental techniques and proposing realistic reaction mechanisms.[18–20] Furthermore, numerous studies on model complexes for oxotransferase enzymes have aimed to deepen the understanding of the natural OAT process.[21–28] These complexes can abstract an oxygen atom from naturally occurring O-donors, such as dimethyl sulfoxide (DMSO)[29] and perchlorate,[30–32] as well as non-biomimetic ones.[33,34] Selected examples of oxotransferase and oxygenase model complexes are shown in Fig. 1.

Molybdenum and tungsten model complexes in the oxidation state +IV exhibiting a MO^{2+} core abstract O-atom from oxygen donors and form MO_2^{2+} species in the oxidation state +VI.[35–37] In a catalytic cycle, the high oxidation state active

---

[a] *Institute of Chemistry, Inorganic Chemistry, University of Graz, 8010 Graz, Austria. E-mail: nadia.moesch@uni-graz.at, miljan.corovic@uni-graz.at*
[b] *BioISI – Instituto de Biossistemas e Ciências Integrativas, Departamento de Química e Bioquímica, Faculdade de Ciências, Universidade de Lisboa, Campo Grande, 1749-016 Lisboa, Portugal. E-mail: mjc@fc.ul.pt, nuno.bandeira@ciencias.ulisboa.pt*

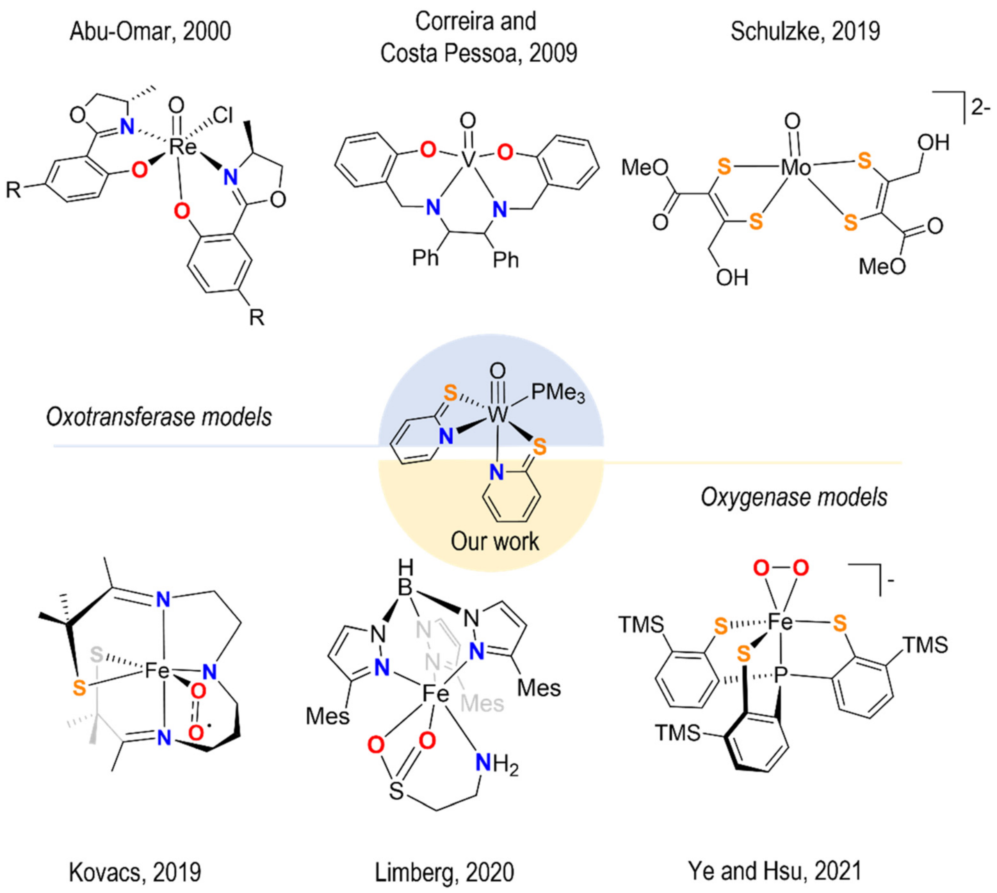

Fig. 1 Selected model complexes for oxotransferase enzymes[29,32,34] (top) and oxygenase enzymes[10,11,15] (bottom). Centrally depicted tungsten(IV) complex activates the substrates of both enzymatic classes.

species must be reduced to MO^{2+}; a process facilitated for MoO_2^{2+} compared to the W analog due to its higher redox potential.[38,39] Therefore, bioinorganic studies on tungsten catalytic cycles are rare, and few Mo *vs.* W comparative studies reveal weaker or no catalytic activity of complexes of the heavier analog.[33,40,41] In recent years, our group has focused on understanding the reduction of WO_2^{2+} with the pyridine-2-thiolate platform (PyS), and we were able to isolate several phosphine-stabilized W(IV) complexes capable of performing oxygen atom transfer with DMSO,[36] H_2O,[42] and O_2.[43] One particular complex, namely $[WO(PyS)_2(PMe_3)_2]$ showed reactivity towards both DMSO, and O_2 (Scheme 1).[43] Both reactions result in the isolation of the corresponding dioxido complex $[WO_2(PyS)_2]$, which, in the presence of a strong reductant such as PMe_3, can regenerate the starting W(IV) compound, enabling catalytic turnover.[36]

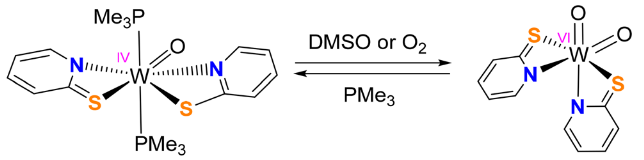

Scheme 1 Oxygen atom transfer reaction between the tungsten(IV) complex $[WO(PyS)_2(PMe_3)_2]$ and DMSO or O_2 leads to the formation of the dioxido tungsten(VI) complex. Back-reaction with PMe_3 leads to the recovery of the starting complex. Side products ($OPMe_3$, and DMS are omitted for clarity).

Reactivity with O_2 was also observed for $[WO(6\text{-}MePyS)_2(PMe_3)_2]$ (6-MePyS = 6-methylpyridine-2-thiolate) which has shown a dynamic behavior in solution, namely a decomplexation of a single phosphine ligand, causing unsaturation and presumably allowing the interaction with a small molecule.[43]

Given that nature does not select W (or Mo) for molecular oxygen activation, this reactivity was unexpected. Although O_2 is not a substrate for W-enzymes, it is known that these enzymes are highly sensitive to oxygen and exhibit their highest performance under anaerobic conditions.[44] Experimental mechanistic studies could not reveal the mechanism of O_2 activation, which prevented elaborate discussion on the behavior of W(IV) compounds, rarely observed as participants of biomimetic OAT cycles. Moreover, investigations of oxidation processes catalyzed by non-noble metals, such as tungsten, provide a valuable alternative to reactions relying on increasingly scarce noble metals.[45,46]

The dual behavior of a single bioinspired complex raises several fundamental questions important for the bioinorganic community. First, why would a diamagnetic platform that favors two-electron transfers activate a paramagnetic small molecule such as O_2? Second, why can two pyridine-2-thiolate ligands support the redox chemistry of WO_2^{2+}, and many other ligands reported in the literature cannot? Finally, is the activation of DMSO, a naturally chosen substrate, energetically more favorable?

To address these questions, this study presents a detailed DFT analysis (calculations with ORCA,[47,48] A/PBE0-D4) combined with a critical evaluation of the previously published experimental data.

Results and discussion

As previously mentioned, dioxygen activation has been observed for $[WO(6\text{-}MePyS)_2(PMe_3)_2]$ (6-MePyS = 6-methylpyridine-2-thiolate) and $[WO(PyS)_2(PMe_3)_2]$ (PyS = pyridine-2-thiolate).[43] Only the latter showed the desired reactivity with DMSO as well,[36] and will therefore be analyzed in this study. Information on the methodology is available in the Computational details given below.

Formation of the active species

The mechanism of O_2 activation occurs *via* the monophosphine variant of the isolated diphosphine compounds ($[WO(6\text{-}MePyS)_2(PMe_3)_2]$ and $[WO(PyS)_2(PMe_3)_2]$). Decoordination of one phosphine ligand has only been observed in solution for the former *via* NMR spectroscopy.[43] However, the dynamic behavior, although to a lower extent, is also assumed for the PyS complex, despite a minor difference in the ligand backbone. To understand the decomplexation of one phosphine ligand the geometry of the di- and monophosphine complexes was optimized for both PyS and 6-MePyS complexes. The calculated structural parameters of the two diphosphine complexes were compared with those obtained experimentally (Table S1 and Fig. S1 in the SI). In $[WO(PyS)_2(PMe_3)_2]$, the seven coordinate metal adopts a pentagonal bipyramidal environment with two κ-S,N PyS ligands. In contrast, in $[W^{IV}O(6\text{-}MePyS)_2(PMe_3)_2]$ the metal is found in a distorted octahedral environment with a κ-S,N and a κ-S 6-MePyS ligand. Indeed, a moderate energy intake ($68.4\ \text{kJ mol}^{-1}$) is required for the system to evolve from $[WO(PyS)_2(PMe_3)_2]$ to the catalytically active species $[WO(PyS)_2(PMe_3)]$ (**A**, Scheme 2). The analogous dissociation for the $[WO(6\text{-}MePyS)_2(PMe_3)_2]$ complex requires just $40.8\ \text{kJ mol}^{-1}$ which explains at least in part why the turnover is higher with this species. The active species **A** is a W(IV) $5d^2$ complex, with a HOMO based on a d_{xy} orbital and the LUMO on a d_{z^2} type orbital. The maximim electron density of the donor and acceptor orbitals indicates where an incoming species will bind (Scheme 2). The HOMO–LUMO gap is 2.95 eV (more details in Fig. S2).

Dioxygen activation

The elementary steps of the reaction between complex $[WO(PyS)_2(PMe_3)]$ (**A**) and dioxygen, leading to the peroxido complex **C**, are presented in Fig. 2. More detailed structural information can be found in the Fig. S3.

In the first step, dioxygen is activated by a closed shell complex **A** with a distorted octahedral structure caused by the very short W–O bond and the bite angles of the bidentate ligands (see Fig. S3). The energy zero is the van der Waals complex formed between complex **A** and dioxygen ($^1\mathbf{A}$ + $^3\mathbf{O_2}$). Energies differ slightly when these "approach" complexes or the free complexes are considered. The coordination environment distorts more upon coordination of the open-shell dioxygen molecule, without changing the bond distances noticeably. First, the $^3O_2$ molecule (triplet state) approaches the metal in the direction of maximum electron density and away from the phosphine (see HOMO in Scheme 2). The metal transfers one 5d electron to one of the half-occupied π* of dioxygen forming a W–O bond, with a barrier of $46\ \text{kJ mol}^{-1}$ ($^3\mathbf{TS_{AB}}$), leading to the higher energy intermediate $^3\mathbf{B}$ ($11\ \text{kJ mol}^{-1}$). The W–O distance decreases from 2.891 Å in the transition state to a long W–O bond of 2.147 Å in $^3\mathbf{B}$. At this stage,

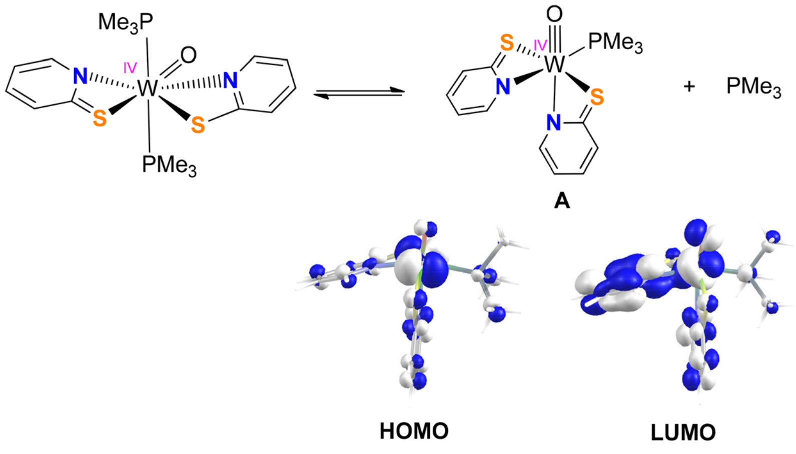

Scheme 2 Dynamic behavior of $[WO(PyS)_2(PMe_3)_2]$ under formation of species $[WO(PyS)_2(PMe_3)]$ (**A**) in solution and frontier orbitals of **A**.

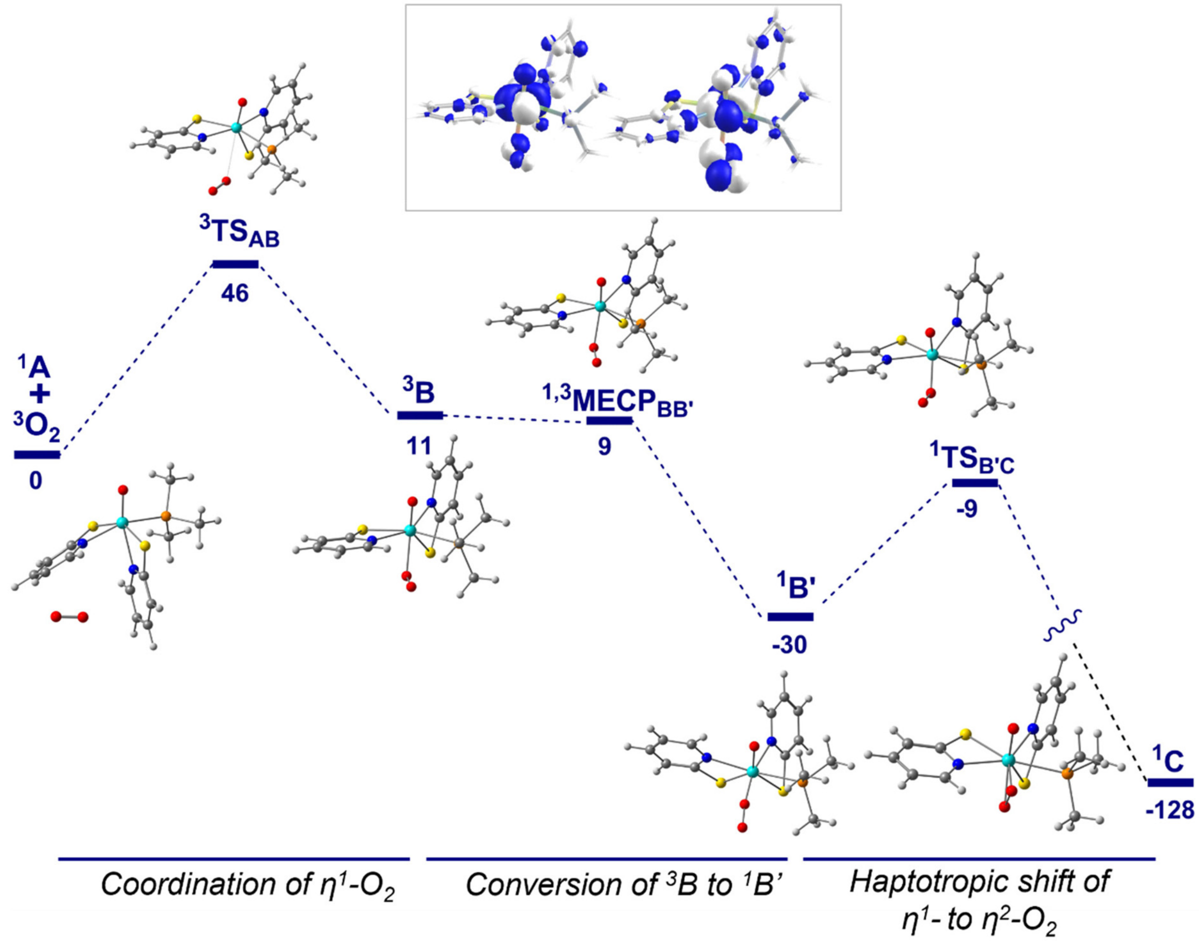

Fig. 2 Dioxygen activation: the interaction of $^3O_2$ with $^1[W(\text{IV})O(PyS)_2(PMe_3)]$ (**A**) and the quasi-restricted single occupied orbitals (SOMOs in the inlet) of the complex at the triplet state of $^{1,3}MECP_{BB'}$ (energies in kJ mol^{-1}).

the metal has been oxidized from W(IV) to W(V) and the O_2 reduced to the superoxide η^1-$(O_2)^-$ (see Fig. 2). Complex ^{3}**B** has the two unpaired electrons with the same spin and each occupying the in and out-of-phase linear combinations $5d_{xy} \pm \pi^*$. Then, the open shell ^{3}**B** intermediate undergoes a spin crossover through the minimum energy crossover point ^{1,3}**MECP** (9 kJ mol^{-1}) leading to a very stable closed shell (singlet) intermediate ^{1}**B′** (−30 kJ mol^{-1}) with a short W–O bond length of 1.785 Å. The ^{1,3}**MECP** exhibits a delocalized electronic structure in the frontier region (inlet in Fig. 2), similarly to the preceding triplet (^{3}**B**), demonstrating that the spin exchange is mediated by tungsten. The O–O distance in $^3\mathbf{TS_{AB}}$ (1.215 Å) is characteristic of an isolated O_2 molecule in the triplet ground state (calculated as 1.189 Å), but after binding, it increases to ~1.30 Å (1.297, 1.292, and 1.286 Å in ^{3}**B**, ^{1,3}**MECP**, and ^{1}**B′**, respectively) indicating, in all these species, the presence of superoxide η^1-$(O_2)^-$ and a formal oxidation change of W(IV) to W(V). The O–O Mayer bond order in ^{3}**B** is 1.3, a close enough value to the theoretically expected 1.5, and the Löwdin bond orders are 1.51 (^{3}**B**) and 1.41 (^{1}**B′**). The spin crossover changes the spin state, but it does not modify these bond lengths and the tungsten(V) oxidation state.

Finally, the coordination mode of O_2 goes from η^1-$(O_2)^-$ to η^2-$(O_2)^{2-}$ over $^1\mathbf{TS_{B'C}}$, as ^{1}**B′** converts to complex $[W(\text{VI})O(\eta^2\text{-}O_2)(PyS)_2(PMe_3)]$ (^{1}**C**). In ^{1}**B′** only one W–O bond (1.785 Å) is formed while the other oxygen atom is more than 3 Å away from the metal. These distances become 1.852 and 2.784 Å in the $^1\mathbf{TS_{B'C}}$ transition state. In ^{1}**C**, the two W–O bond lengths are the same (1.968 Å) and the long O–O distance of 1.445 Å characterizes a bound peroxido ligand. Also, the Löwdin bond order is only 1.13, reflecting a much weaker O–O bond than in the superoxide. In summary, the activation of dioxygen takes place in two consecutive one-electron steps, starting from W(IV) and O_2, *via* W(V) and η^1-$(O_2)^-$, and finally reaching W(VI) and η^2-$(O_2)^{2-}$. Although complex ^{1}**C** is extremely stable (−128 kJ mol^{-1}), catalytic PMe_3 oxidation is still occurring.

From η^2-peroxido to dioxido complex

All the following reactions involve diamagnetic molecules and therefore the spin state is not indicated (*e.g.* **C** rather than ^{1}**C**). There are several possibilities to reach the isolated dioxido complex $[WO_2(PyS)_2]$ starting from the η^2-peroxido species $[WO(\eta^2\text{-}O_2)(PyS)_2(PMe_3)]$ (**C**), since it contains two different oxygen sources (oxido and peroxido) and two different phosphines (coordinated to W and free in solution during the catalytic reaction). Our study reveals that the attack by an external phosphine at the coordinated peroxido ligand in **C** represents the least energy demanding process (outer-sphere mechanism, Fig. 3 and Fig. S4), and is therefore here discussed in detail. Other mechanistic scenarios, involving the free phosphine attacking the oxide or the coordinated phosphine attacking either the peroxide or the oxide (inner-sphere mechanism), are less likely to occur owing to the larger energies required.

In the more favorable outer-sphere mechanism, the free phosphine approaches one of the coordinated oxygen atoms of the peroxido ligand in **C** (Fig. 3). In the transition state **TS_{CD}**, the P–O distance is 2.312 Å and decreases to 1.518 Å in the free phosphine oxide. Simultaneously, the O–O bond increases from 1.445 Å in **C** to 1.698 Å in **TS_{CD}**, being completely cleaved in the intermediate **D**. The formation of the P–O and the cleavage of the O–O bonds occur simultaneously as shown in Fig. 3, with a barrier of 93 kJ mol^{-1}. The phosphine oxide is formed and released in one step. Intermediate **D** is a sterically crowded seven-coordinate W(VI) complex with a very low energy, where W(VI) forms much weaker bonds with P ligands than W(IV).[49] Thus, **D** can lose the remaining phosphine, passing over transition states **TS_{DE}** and **TS_{EF}** with barriers of 70 and 16 kJ mol^{-1}, to successively afford two isomers of the dioxido complex **E** and **F** (Fig. 3). Overall, the activation energy for the loss of phosphine is lower than **TS_{CD}** (93 kJ mol^{-1}), where the reaction takes place, while the isomerization requires a much smaller energy.

The description and comparison of alternative outer and inner sphere mechanisms can be found in the (Fig. S5–S10). The dioxido complex [$WO_2(PyS)_2$] is a distorted octahedral complex, with several isomers (I#), namely intermediates **E** and **F** in Fig. 3. Furthermore, the possible isomer **I1** was previously crystallographically determined[36] and was found to be the most stable one (details about these isomers and their interconversion are given in Fig. S11 and in the SI). Our study shows that these isomers interconvert with small barriers as expected for a d^0 species.

Reduction to W(IV) and closing the catalytic cycle

The dioxido complex **F** [$WO_2(PyS)_2$] must convert to complex **A** [$WO(PyS)_2(PMe_3)$] to close the catalytic cycle (Fig. 4 and

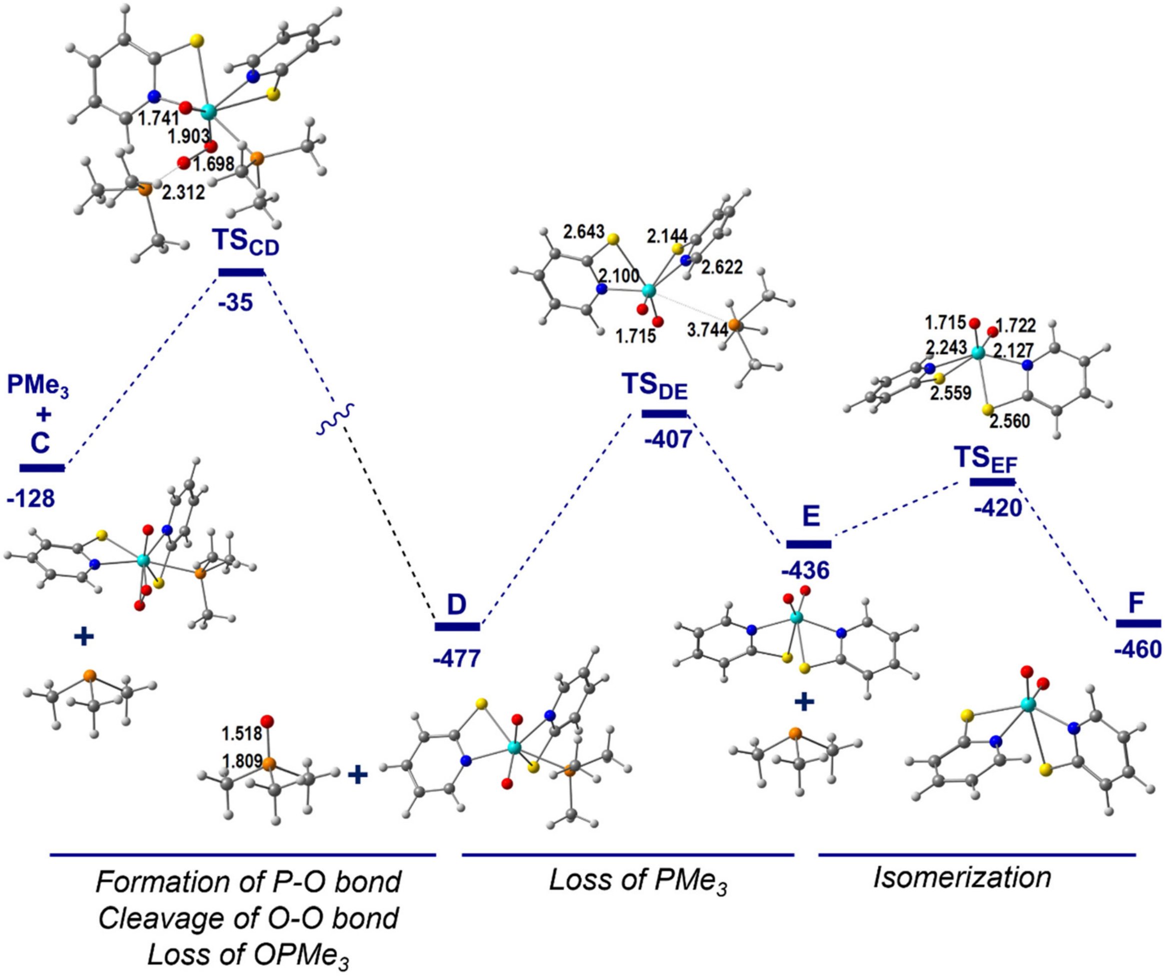

Fig. 3 Outer-sphere mechanism for attack of PMe_3 at the peroxide of [$WO(\eta^2\text{-}O_2)(PyS)_2(PMe_3)$] (**C**) (distances in Å, energies in kJ mol^{-1}).

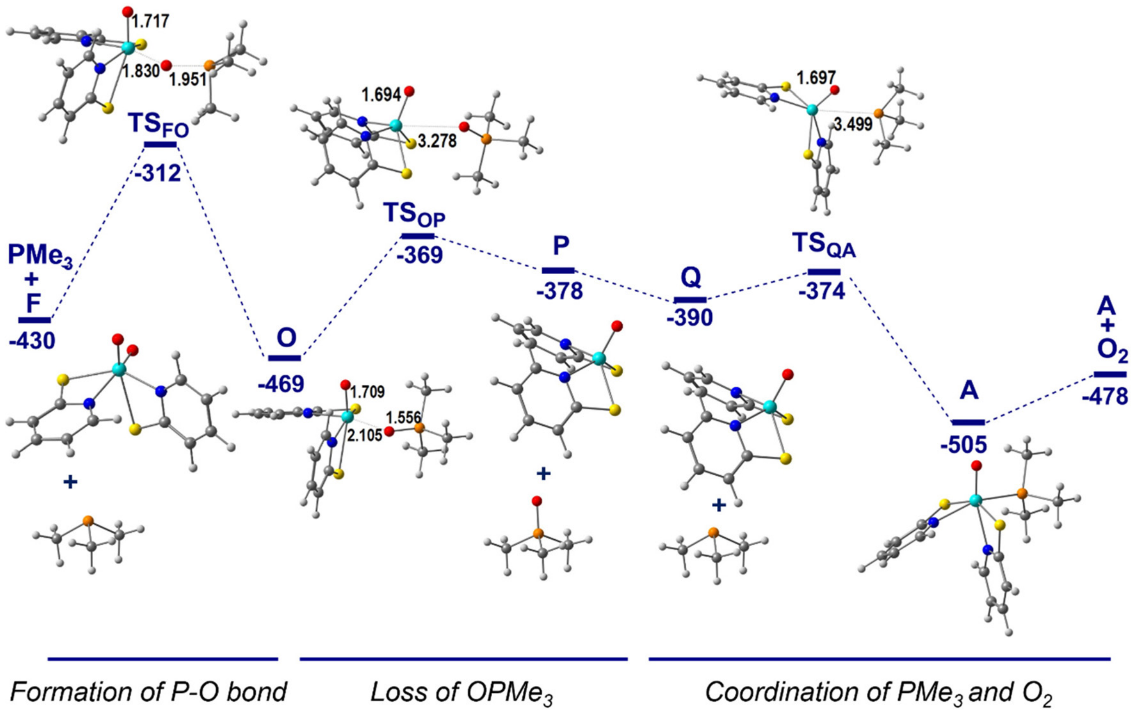

Fig. 4 Closing of the catalytic cycle and regeneration of the $[WO(PyS)_2(PMe_3)]$ (**A**). The final product **A** + O_2 corresponds to the beginning of the reaction in Fig. 2 (distances in Å, energies in kJ mol^{-1}).

Fig. S12 in the SI). The reduction of W(VI) to W(IV) is achieved by the oxidation of the phosphine, which approaches one of the oxygen atoms *via* the transition state $\mathbf{TS_{FO}}$ with the W–O and O–P distances of 1.830 and 1.951 Å, respectively. In the subsequent intermediate **O**, the $OPMe_3$ molecule must be released. The dissociation requires a rearrangement *via* $\mathbf{TS_{OP}}$ to afford the monoxido complex $[WO(PyS)_2]$ weakly bound (van der Waals interaction) in **P**. Finally, the $[WO(PyS)_2]$ approaches PMe_3 (**Q**) and regenerates the starting tungsten(IV) complex **A** with a very low barrier (16 kJ mol^{-1}). Complex **A** can then be approached by O_2 to initiate the next catalytic cycle (Fig. 2).

The thermodynamics of the catalytic cycle is shown in the equations below (energies in kJ mol^{-1}). Notice that these reactions are not exactly the same as in Fig. 2, 3 and 4, since the other intermediates cancel out and all the complexes are isolated.

It is noteworthy that the energy released upon phosphine oxidation drives tungsten reduction and allows for the catalytic cycle (Fig. 5).

Starting from the reaction between **A** and dioxygen (reaction energy zero as shown in Fig. 5), high activation energies are observed in two steps involving oxygen atom transfer reactions to PMe_3. The first oxidant is the complex $[WO(O)_2(PyS)_2(PMe_3)]$ (**C**) (93 kJ mol^{-1}, Fig. 3) where the peroxido ligand receives two electrons therefore splitting into two O^{2-} ions. In the second PMe_3 oxidation, the reduction of WO_2^{2+} in $[WO_2(PyS)_2]$ (**F**) to WO^{2+} in $[WO(PyS)_2]$ (**O**), is even more energy-demanding (118 kJ mol^{-1}, Fig. 4).

Moreover, the formation of the monoxido complex $[WO(PyS)_2]$ could cause the comproportionation with the dioxido complex **F** $[WO_2(PyS)_2]$ to a binuclear species $[\{WO(PyS)_2\}_2(\mu\text{-}O)]$ (**R**, Fig. S13 in the SI). The W dimer is surprisingly stable

$[WO(PyS)_2(PMe_3)]$ (**A**) + O_2 → $[WO(O)_2(PyS)_2(PMe_3)]$ (**C**) **1** -101

$[WO(O)_2(PyS)_2(PMe_3)]$ (**C**) + PMe_3 → $[WO_2(PyS)_2]$ (**F**) + PMe_3 + $OPMe_3$ **2** -332

$[WO_2(PyS)_2]$ (**F**) + PMe_3 → $[WO(PyS)_2]$ + $OPMe_3$ **3** +57

$[WO(PyS)_2]$ + PMe_3 → $[WO(PyS)_2(PMe_3)]$ (**A**) **4** -102

2 PMe_3 + O_2 → 2 $OPMe_3$ **1 + 2 +3 + 4 = -478**

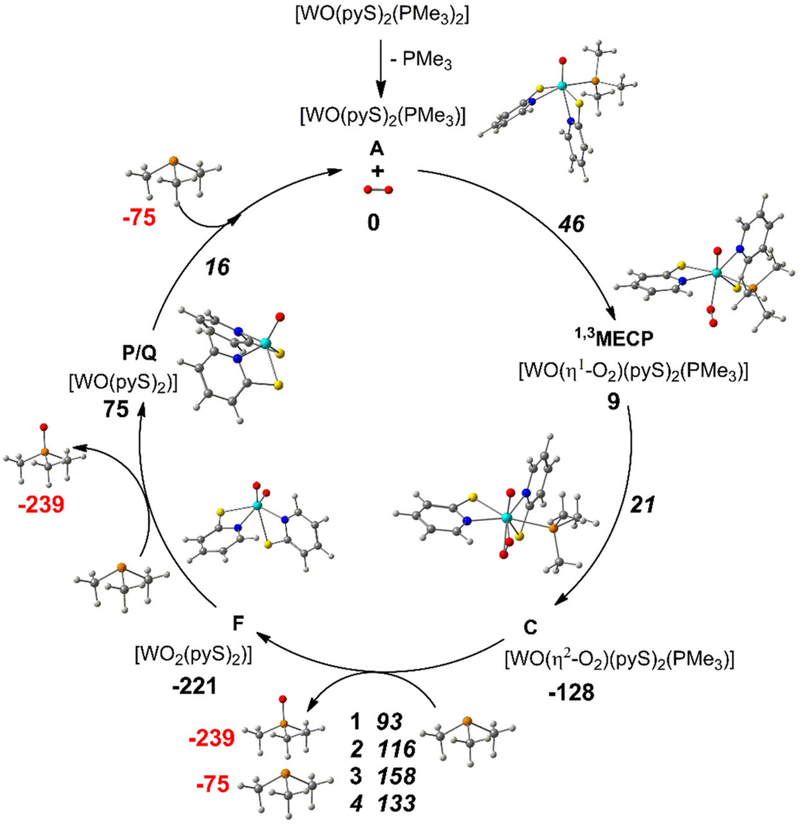

Fig. 5 Calculated catalytic cycle for aerobic oxidation of PMe_3 catalyzed by tungsten(IV) $[WO(PyS)_2(PMe_3)]$ (**A**) (1, 2, 3, 4 refer to the four mechanisms fully described in Fig. 3, S5, S7 and S9 in the SI). (Energies in kJ mol^{-1}, ΔG bold, $\Delta G^{\ddagger}$ bold italic).

(-100 kJ mol^{-1}) and the barrier to its formation is only 29 kJ mol^{-1}. This type of reactivity is often observed in Mo chemistry, where the dimeric resting state interferes with the catalytic cycle.[31] The Mo complex $[MoO(PyS)_2]$ and the **F** analogue react similarly, with a slightly smaller barrier (Fig. S13 in the SI). Although the formation of dimeric species is theoretically possible, the unsaturated complex most likely reacts with O_2 or PMe_3, under catalytic conditions (excess O_2 or PMe_3). No dinuclear species were detected for tungsten under catalytic conditions or in the absence of oxidants.[36,43]

DMSO activation

In nature, molybdoenzyme DMSO reductase reduces DMSO to dimethylsulfide (DMS). Also a tungsten variant of the enzyme was found to be active toward DMSO reduction.[50,51] As previously described,[36] complex **A** also undergoes an OAT reaction with DMSO. Therefore, we analyzed this transformation computationally to compare it to dioxygen activation.

The energy profile for the reaction is shown in Fig. 6 (detailed structural analysis is given in Fig. S14). After the formation of the contact complex (**A** +DMSO), a W–O bond starts to appear at $\mathbf{TS_{AS}}$, with a long W–O distance of 3.047 Å and a S–O bond only slightly longer than in the free molecule. Going from intermediate **S** to **T**, the W–O distance decreases from 2.329 Å (W–O–S in **S**), over 1.944 Å (in $\mathbf{TS_{ST}}$) to 1.728 Å (W═O bond in **T**). Simultaneously, the O–S distance increases to 1.548, 1.831, and 3.937 Å, as the S═O bond weakens and finally breaks, releasing DMS. The activation energies are 26 and 19 kJ mol^{-1}, the higher one being associated with the formation of the new W–O bond and the smaller one with cleaving the S–O bond. In the process, sulfur is reduced and tungsten is directly oxidized from W(IV) to W(VI). As expected, the oxidation with DMSO requires less energy than with O_2, but even in this case, the steps of the catalytic cycle with the highest barriers were found in the tungsten reduction steps (Fig. 6).

Discussion

To explain the unusual reactivity of the diamagnetic tungsten center with dioxygen, a simplified reaction pathway is shown in Scheme 3 (top). Additionally, a simplified representation of the first coordination sphere of selected intermediates is shown, illustrating the orientation of the two PyS ligands with the W═O unit fixed (Scheme 3, bottom).

Although W(IV) complex A is diamagnetic, it can bind dioxygen in an end-on fashion leading to the one-electron oxidation of tungsten center to the high energy triplet state tungsten(V)-superoxido intermediate ^{3}**B**. A spin-crossover, mediated by the tungsten center, converts ^{3}**B** to a much more stable diamagnetic tungsten(V)-superoxido species ^{1}**B′**. A second electron transfer leads to W(VI). In biological systems, such a process is

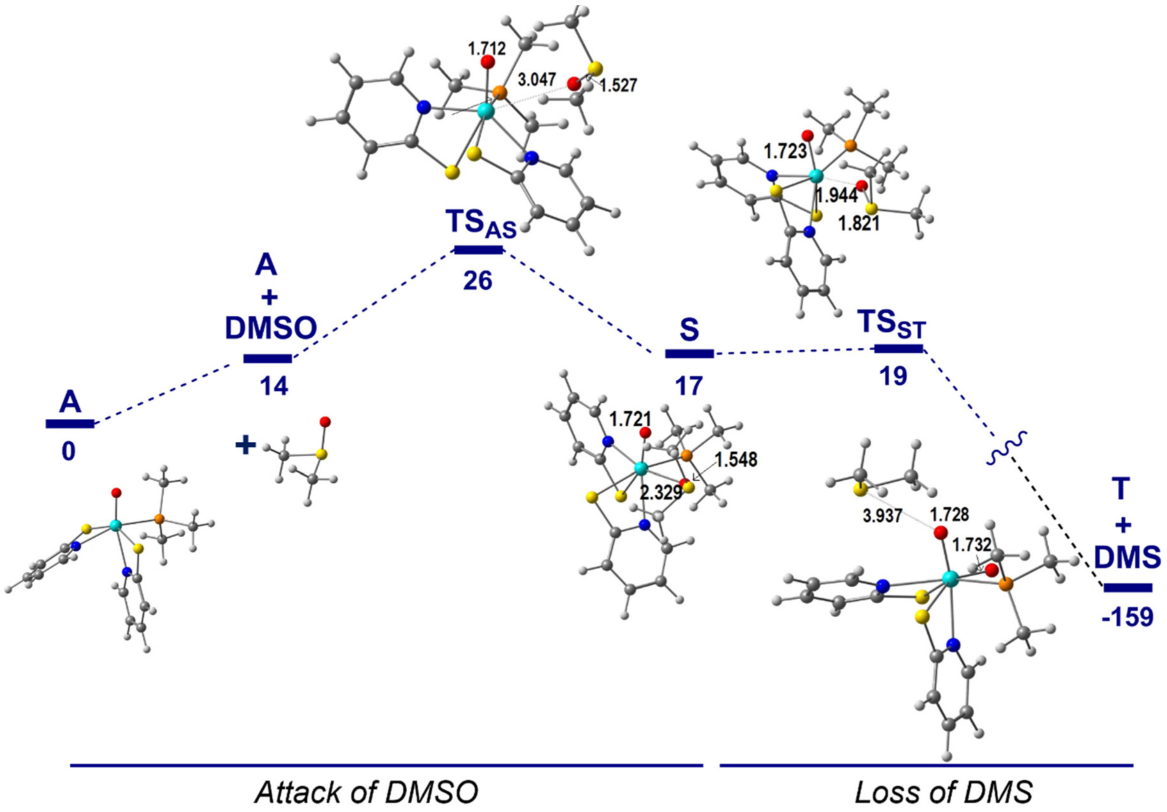

Fig. 6 Activation of DMSO by and $[WO(PyS)_2(PMe_3)]$ (**A**) (distances in Å, energies in kJ mol^{-1}).

not observed during the OAT process as tungsten directly reaches its highest oxidation state.[52,53] However, the recovery of the tungsten center occurs *via* two cycles of proton-coupled electron transfer (PCET) which involves the intermediate formation of W(V).[54]

With a small energy cost (46 kJ mol^{-1}), dioxygen coordination leads to the formation of a more stable peroxido complex ^{1}**C** (−128 kJ mol^{-1}). Subsequent reactions with phosphine yield the dioxido complex **F**, which serves as a thermodynamic anchor in the reaction. Ultimately, the high stability of the WO_2^{2+} moiety is the driving force of the overall process of dioxygen activation.

Our findings demonstrate a strong tendency for dioxygen activation at high-valent tungsten centers, challenging their general underrepresentation in aerobic catalysis. The low redox potential of tungsten often limits its catalytic performance compared to molybdenum in redox reactions.[54] In our system, the enhanced reducibility of the otherwise stable tungsten dioxido complexes is attributed to the coordinative flexibility of the pyridine-2-thiolate ligands. Structural analysis of the calculated species participating in the studied catalytic cycle reveals significant conformational changes upon reduction as presented in Scheme 3. To describe changes in the relative orientation of the two planar ancillary ligands during the catalytic cycle, we examined the *S*,*S*- and *N*,*N*-arrangements, specifically distinguishing between *cis*- and *trans*-configurations. The most significant changes in ligand orientation are observed upon a change in coordination number from six to seven, such as during O_2 coordination, or upon formation of the six-coordinate dioxido complex. The dynamic behavior of the chosen ligand system enables access to different spin states of the tungsten center, facilitating the activation of both DMSO (oxotransferase substrate) and O_2 (oxygenase substrate). Similarly, in biological systems, the dithiolene coordination sphere of Mo and W metalloprotein cofactors is known for its conformational flexibility, which supports the diverse oxidation states of the central tungsten and therefore allows both one- and two-electron transfers.[55–57] Moreover, tungsten enzymes are frequently inactivated under aerobic conditions,[44] which has been attributed to the oxidative degradation of associated [4Fe–4S] clusters—as seen in enzymes where exposure to air leads to their conversion into [3Fe–4S] forms.[58,59] Therefore, our findings suggest how O_2 could bind to W(IV) in biological environment.

Although the dual reactivity observed in our system is interesting, it is very unlikely that nature would favor molybdenum or tungsten over *e.g.*, iron for dioxygen activation and challenging oxidation reactions. The limitations are their low bioavailability (for W), diamagnetic resting states, and the high stability of their higher oxidation states (which requires a very strong reductant). In contrast, iron enzymes, when reacting with dioxygen, produce reactive high-valent species capable of

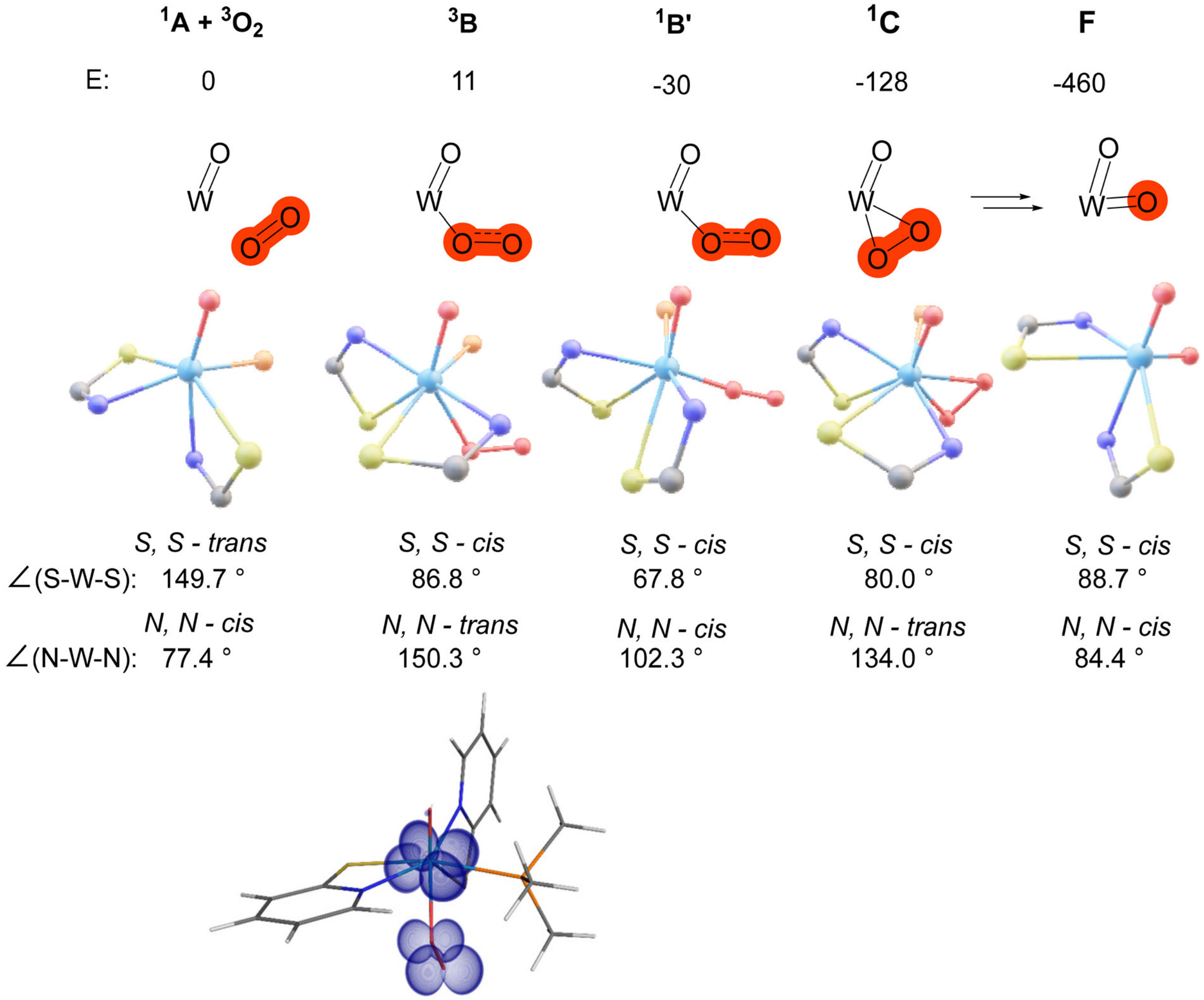

Scheme 3 Top: simplified reaction pathway between complex **A** and dioxygen, leading to the formation of the dioxido complex **F** (energies in kJ mol^{-1}). Bottom: representation of the first coordination sphere highlighting the mutual orientation of the PyS ligands, along with S–W–S and N–W–N angles. In addition, a spin density picture of complex ^{3}**B** shows that one electron is localized at the W-center and another at the η^1-(O_2) moiety.

oxidizing challenging substrates.[60,61] Therefore, nature chose Mo and W for their ability to facilitate challenging reductions. Mo- and W-dependent oxotransferases use the high-energy nature of their reduced states to drive the reduction of otherwise inert compounds, such as perchlorate or nitrate.[6,44,62,63]

Conclusions

Unusual reactivity of bioinspired unsaturated tungsten(IV) complex **A**, [WO(PyS)$_2$(PMe$_3$)], which can activate both O_2 and DMSO, inspired a detailed computational study of this dual behavior. We discovered that DMSO activation occurs *via* a simple OAT mechanism, closely resembling the process in nature for tungsten-containing oxotransferase enzymes. In contrast, dioxygen activation proceeds through the formation of a paramagnetic tungsten(V)-superoxido intermediate, which, though similar to oxygenase enzyme intermediates, had not been previously observed for tungsten. Subsequent steps, involving a spin crossover to a diamagnetic tungsten(V)-superoxido complex, and a coordination rearrangement of η^1-O_2 to η^2-O_2, lead to the formation of a W(VI)-peroxide and an exceptionally stable dioxido complex, which serves as the thermodynamic driving force for the overall reaction. The one-electron oxidation of the tungsten center is atypical, as third-block transition metals usually undergo two-electron transfers. However, this was made possible by the coordinative flexibility of the two bidentate pyridine-2-thiolate ligands, allowing one O atom of O_2 to bind selectively end-on at the electronically favored position and therefore accepting only one electron. In conclusion, designing a new tungsten-based redox catalyst requires a flexible ligand scaffold to enable reduction of the WO_2^{2+} moiety. The regeneration of the catalyst from the very stable W(VI) dioxido complex is achieved by two phosphine molecules, one of them needed to complete the coordination sphere of the active species **A**, and the second one to reduce the metal to W(IV) with high barriers.

Computational details

The ORCA[47,48] software package version 5.0.4 was used throughout. The geometries of the complexes were based on those obtained by single crystal X-ray diffraction.[36,43] The hybrid GGA class PBE0 exchange–correlation functional by Adamo and Barone,[64,65] was employed as density functional approximation augmented by Grimme's fourth generation dispersion correction (PBE0-D4).[66–68]

All electron relativistic basis sets of the X2C family,[69,70] were used namely X2C-TZVPall for W and X2C-SVPall for the remaining atoms. The Douglas–Kroll–Heβ[71–73] relativistic Hamiltonian truncated at second order (DKH2) was used in the calculations. The multi-center integrals were approximated by the RIJCOSX[74–77] technique with automatically generated auxiliary basis sets.[78] A Gaussian finite nucleus model[78] was employed in the calculations to account for atomic size effects. Solvent effects were accounted for by the conductor-like polarizable continuum model[79,80] (C-PCM) with default parameters for dichloromethane (CH$_2$Cl$_2$). Orbitals and structures were rendered with Chemcraft.[81]

Author contributions

MZĆ discussed the results and assisted in the manuscript preparation. MJC discussed the results and assisted in the manuscript preparation and its revision. NAGB conceived the project, performed the DFT calculations and revised the manuscript. NMZ discussed the results, assisted and revised the manuscript. CRediT: MZĆ formal analysis, visualization, writing – review & editing; MJC data curation, visualization, writing-original draft, formal analysis; NAGB investigation, conceptualization, validation, supervision, resources, formal analysis; NMZ project administration, funding acquisition, writing-review and editing. All authors contributed and have given approval to the final version of the manuscript.

Conflicts of interest

There are no conflicts to declare.

Data availability

Computational data (optimized geometries and orbitals), and the description of alternative reaction mechanisms (.pdf) and an xyz file with the coordinates of all optimized species are given in the supplementary information. See DOI: **https://doi.org/10.1039/d5dt01544h**.

Acknowledgements

NAGB acknowledges funding by the following entities: Fundação para a Ciência e a Tecnologia through BioISI research unit funding UID/04046/2025 (**https://doi.org/10.54499/UIDB/04046/2020**, **https://doi.org/10.54499/UIDP/04046/2020**), DL57 individual researcher funding (**https://doi.org/10.54499/DL57/2016/CP1479/CT0050**) and additionally project grant PTDC/QUI-QIN/0252/2021 (**https://doi.org/10.54499/PTDC/QUI-QIN/0252/2021**). NAGB gratefully acknowledges Prof. Frank Neese for providing access to computational infrastructure. MZĆ and NMZ acknowledge the financial support by the University of Graz, Austria.

References

1 A. D. Anbar, *Science*, 2008, **322**, 1481–1483.
2 C. L. Dupont, A. Butcher, R. E. Valas, P. E. Bourne and G. Caetano-Anollés, *Proc. Natl. Acad. Sci. U. S. A.*, 2010, **107**, 10567–10572.
3 H. Sigel and A. Sigel, *Z. Naturforsch., B: J. Chem. Sci.*, 2019, **74**, 461–471.
4 M. L. Kirk and K. C. Khadanand, in *Metal Ions in Life Sciences*, ed. M. Sosa Torres and P. Kroneck, De Gruyter, 2020, pp. 313–342.
5 R. Hille, C. Schulzke and M. L. Kirk, in *RSC Metallobiology Series*, The Royal Society of Chemistry, Cambridge, UK, 2017.
6 S. Pätsch, J. V. Correia, B. J. Elvers, M. Steuer and C. Schulzke, *Molecules*, 2022, **27**, 3695.
7 M. M. Abu-Omar, A. Loaiza and N. Hontzeas, *Chem. Rev.*, 2005, **105**, 2227–2252.
8 R. Hille, *Chem. Rev.*, 1996, **96**, 2757–2816.
9 R. Zhao, B.-B. Zhang, Z. Liu, G.-J. Cheng and Z.-X. Wang, *JACS Au*, 2022, **2**, 745–761.
10 M. N. Blakely, M. A. Dedushko, P. C. Yan Poon, G. Villar-Acevedo and J. A. Kovacs, *J. Am. Chem. Soc.*, 2019, **141**, 1867–1870.
11 H.-R. Pan, H.-J. Chen, Z.-H. Wu, P. Ge, S. Ye, G.-H. Lee and H.-F. Hsu, *JACS Au*, 2021, **1**, 1389–1398.
12 D. Kass, T. Corona, K. Warm, B. Braun-Cula, U. Kuhlmann, E. Bill, S. Mebs, M. Swart, H. Dau, M. Haumann, P. Hildebrandt and K. Ray, *J. Am. Chem. Soc.*, 2020, **142**, 5924–5928.
13 M. R. Bukowski, K. D. Koehntop, A. Stubna, E. L. Bominaar, J. A. Halfen, E. Münck, W. Nam and L. Que, *Science*, 2005, **310**, 1000–1002.
14 W. Nam, *Acc. Chem. Res.*, 2007, **40**, 522–531.
15 L. Müller, S. Hoof, M. Keck, C. Herwig and C. Limberg, *Chem. – Eur. J.*, 2020, **26**, 11851–11861.
16 J. Ackermann, F. Meyer, E. Kaifer and H. Pritzkow, *Chem. – Eur. J.*, 2002, **8**, 247–258.
17 A. Arnold, C. Limberg and R. Metzinger, *Inorg. Chem.*, 2012, **51**, 12210–12217.
18 G. Dong and U. Ryde, *Inorg. Chem.*, 2016, **55**, 11727–11735.
19 M. Swart and M. Reimann, *SciPost Chem.*, 2024, **3**, DOI: **10.21468/SciPostChem.3.1.001**.
20 N. J. Britto, M. Jaccob, P. Comba, K. Anandababu and R. Mayilmurugan, *J. Inorg. Biochem.*, 2023, **238**, 112066.
21 C. Schulzke, *Eur. J. Inorg. Chem.*, 2011, **2011**, 1189–1199.

22 M. A. Ehweiner, F. Wiedemaier, B. Lajin, J. A. Schachner, F. Belaj, W. Goessler and N. C. Mösch-Zanetti, *ACS Catal.*, 2021, **11**, 11754–11761.

23 S. B. Yu and R. H. Holm, *Inorg. Chem.*, 1989, **28**, 4385–4391.

24 J. Li and U. Ryde, *Inorg. Chem.*, 2014, **53**, 11913–11924.

25 J. M. Berg and R. H. Holm, *J. Am. Chem. Soc.*, 1985, **107**, 917–925.

26 C. A. Canote and S. M. Kilyanek, *Dalton Trans.*, 2024, **53**(11), 4874–4889.

27 K. Heinze, *Coord. Chem. Rev.*, 2015, **300**, 121–141.

28 A. Majumdar, *Dalton Trans.*, 2014, **43**, 8990–9003.

29 M. Ahmadi, C. Fischer, A. C. Ghosh and C. Schulzke, *Front. Chem.*, 2019, **7**, 486.

30 C. L. Ford, Y. J. Park, E. M. Matson, Z. Gordon and A. R. Fout, *Science*, 2016, **354**, 741–743.

31 R. Bondi, M. A. Ehweiner, F. Belaj and N. C. Mösch-Zanetti, *J. Catal.*, 2022, **416**, 344–351.

32 M. M. Abu-Omar, L. D. McPherson, J. Arias and V. M. Béreau, *Angew. Chem., Int. Ed.*, 2000, **39**, 4310–4313.

33 F. R. Neururer, F. Heim, M. Baltrun, P. Boos, J. Beerhues, M. Seidl and S. Hohloch, *Inorg. Chem. Front.*, 2025, **12**, 2224–2235.

34 P. Adão, J. Costa Pessoa, R. T. Henriques, M. L. Kuznetsov, F. Avecilla, M. R. Maurya, U. Kumar and I. Correia, *Inorg. Chem.*, 2009, **48**, 3542–3561.

35 M. A. Ehweiner, F. Wiedemaier, F. Belaj and N. C. Mösch-Zanetti, *Inorg. Chem.*, 2020, **59**, 14577–14593.

36 M. Z. Ćorović, F. Wiedemaier, F. Belaj and N. C. Mösch-Zanetti, *Inorg. Chem.*, 2022, **61**, 12415–12424.

37 P. Basu, B. W. Kail and C. G. Young, *Inorg. Chem.*, 2010, **49**, 4895–4900.

38 A. Döring and C. Schulzke, *Dalton Trans.*, 2010, **39**, 5623–5629.

39 G. C. Tucci, J. P. Donahue and R. H. Holm, *Inorg. Chem.*, 1998, **37**, 1602–1608.

40 J. A. Schachner, N. C. Mösch-Zanetti, A. Peuronen and A. Lehtonen, *Polyhedron*, 2017, **134**, 73–78.

41 Y.-L. Wong, L. H. Tong, J. R. Dilworth, D. K. P. Ng and H. K. Lee, *Dalton Trans.*, 2010, **39**, 4602–4611.

42 M. Z. Ćorović, A. Milinkovic, N. Stix, A. Dupé and N. C. Mösch-Zanetti, *Inorg. Chem.*, 2024, **63**, 11953–11962.

43 M. Z. Ćorović, F. Belaj and N. C. Mösch-Zanetti, *Inorg. Chem.*, 2023, **62**, 5669–5676.

44 C. M. Cordas and J. J. Moura, *Coord. Chem. Rev.*, 2019, **394**, 53–64.

45 C. Nickel, D. L. Troglauer, Z. Dallos, D. Abid, K. Sowa, M. O. Cichocka, U. Kolb, B. Mashtakov, B. F. Mohazzab, S. Han, L. Prädel, L. Ci, D. Li, X. Lin, M. Hua, R. Liu and D. Gao, *Angew. Chem., Int. Ed.*, 2025, e202424074.

46 H. Song, J. Wei, Z. Wang, Y. Liu, S. Zhao, X. Cai, Y. Xiao, L. Yang, P. Bai, L. Fang, F. Yang, S. Zheng, W. Zhang, J. Pan and C. Xu, *ACS Catal.*, 2024, **14**, 12372–12384.

47 F. Neese, *J. Comput. Chem.*, 2023, **44**, 381–396.

48 F. Neese, *Wiley Interdiscip. Rev.: Comput. Mol. Sci.*, 2022, **12**, e1606.

49 R. G. Pearson, *J. Am. Chem. Soc.*, 1963, **85**, 3533–3539.

50 J. Pacheco, D. Niks and R. Hille, *J. Biol. Inorg. Chem.*, 2018, **23**, 295–301.

51 L. J. Stewart, S. Bailey, B. Bennett, J. M. Charnock, C. D. Garner and A. S. McAlpine, *J. Mol. Biol.*, 2000, **299**, 593–600.

52 A. L. Tenderholt, R. K. Szilagyi, R. H. Holm, K. O. Hodgson, B. Hedman and E. I. Solomon, *J. Inorg. Biochem.*, 2007, **101**, 1594–1600.

53 Y. Ha, A. L. Tenderholt, R. H. Holm, B. Hedman, K. O. Hodgson and E. I. Solomon, *J. Am. Chem. Soc.*, 2014, **136**, 9094–9105.

54 R. H. Holm, *Coord. Chem. Rev.*, 1990, **100**, 183–221.

55 R. A. Rothery, B. Stein, M. Solomonson, M. L. Kirk and J. H. Weiner, *Proc. Natl. Acad. Sci. U. S. A.*, 2012, **109**, 14773–14778.

56 S. J. N. Burgmayer and M. L. Kirk, *Molecules*, 2023, **28**(22), 7456.

57 H. K. Joshi, J. J. A. Cooney, F. E. Inscore, N. E. Gruhn, D. L. Lichtenberger and J. H. Enemark, *Proc. Natl. Acad. Sci. U. S. A.*, 2003, **100**, 3719–3724.

58 R. U. Meckenstock, R. Krieger, S. Ensign, P. M. Kroneck and B. Schink, *Eur. J. Biochem.*, 1999, **264**, 176–182.

59 F. Tenbrink, B. Schink and P. M. H. Kroneck, *J. Bacteriol.*, 2011, **193**, 1229–1236.

60 T. M. Makris, K. von Koenig, I. Schlichting and S. G. Sligar, *J. Inorg. Biochem.*, 2006, **100**, 507–518.

61 P. Hosseinzadeh and Y. Lu, *Biochim. Biophys. Acta, Bioenerg.*, 2016, **1857**, 557–581.

62 U. Das, A. Das and A. K. Das, *Coord. Chem. Rev.*, 2025, **523**, 216290.

63 L. B. Maia, I. Moura and J. J. G. Moura, in *Molybdenum and Tungsten Enzymes: Biochemistry*, ed. R. Hille, C. Schulzke and M. Kirk, Royal Society of Chemistry, Cambridge, UK, 2017, pp. 1–80.

64 C. Adamo and V. Barone, *Chem. Phys. Lett.*, 1998, **298**, 113–119.

65 C. Adamo, M. Cossi, G. Scalmani and V. Barone, *Chem. Phys. Lett.*, 1999, **307**, 265–271.

66 E. Caldeweyher, C. Bannwarth and S. Grimme, *J. Chem. Phys.*, 2017, **147**, 34112.

67 E. Caldeweyher, S. Ehlert, A. Hansen, H. Neugebauer, S. Spicher, C. Bannwarth and S. Grimme, *J. Chem. Phys.*, 2019, **150**, 154122.

68 E. Caldeweyher, J.-M. Mewes, S. Ehlert and S. Grimme, *Phys. Chem. Chem. Phys.*, 2020, **22**, 8499–8512.

69 P. Pollak and F. Weigend, *J. Chem. Theory Comput.*, 2017, **13**, 3696–3705.

70 Y. J. Franzke, R. Treß, T. M. Pazdera and F. Weigend, *Phys. Chem. Chem. Phys.*, 2019, **21**, 16658–16664.

71 M. Douglas and N. M. Kroll, *Ann. Phys.*, 1974, **82**, 89–155.

72 B. A. Hess, *Phys. Rev. A*, 1986, **33**, 3742–3748.

73 G. Jansen and B. A. Hess, *Phys. Rev. A*, 1989, **39**, 6016–6017.

74 F. Neese, *J. Comput. Chem.*, 2003, **24**, 1740–1747.

75 B. Helmich-Paris, B. de Souza, F. Neese and R. Izsák, *J. Chem. Phys.*, 2021, **155**, 104109.

76 R. Izsák and F. Neese, *J. Chem. Phys.*, 2011, **135**, 144105.

77 F. Neese, F. Wennmohs, A. Hansen and U. Becker, *Chem. Phys.*, 2009, **356**, 98–109.

78 G. L. Stoychev, A. A. Auer and F. Neese, *J. Chem. Theory Comput.*, 2017, **13**, 554–562.

79 L. Visscher and K. G. Dyall, *At. Data Nucl. Data Tables*, 1997, **67**, 207–224.

80 M. Garcia-Ratés and F. Neese, *J. Comput. Chem.*, 2019, **40**, 1816–1828.

81 Chemcraft Version 1.8. Graphical software for visualization of quantum chemistry computations. build 682.